

Strong and ductile CoCrFeNi high-entropy alloy microfibers at ambient and cryogenic temperatures

Xiaoyu Gao^a, Jian Liu^b, Wujing Fu^a, Yongjiang Huang^{a,*}, Zhiliang Ning^a, Zhixiong Zhang^c, Jianfei Sun^a, Wen Chen^{b,*}

^a School of Materials Science and Engineering, Harbin Institute of Technology, Harbin 150001, China

^b Department of Mechanical and Industrial Engineering, University of Massachusetts Amherst, MA 01003, USA

^c College of Mechanical and Vehicle Engineering, Taiyuan University of Technology, Taiyuan 030024, China

ARTICLE INFO

Keywords:
High entropy alloy
Microfiber
Mechanical properties
Cryogenic temperature
Microstructure

ABSTRACT

Exploring metallic microfibers with an excellent combination of high strength and ductility is a challenge for structural applications under extreme conditions. In this work, a heterogeneous gradient structure was introduced into CoCrFeNi high-entropy alloy (HEA) microfibers via thermomechanical processing. The annealed CoCrFeNi microfiber displays an ultrahigh yield strength of ~ 1 GPa, an ultimate tensile strength of 1.45 GPa, and an outstanding uniform elongation of 75% at 150 K. These excellent properties originate from the ultrafine grains and heterogeneous gradient structure, as well as the activation of multiple deformation mechanisms including deformation twins, dense dislocations, stacking faults, Lomer-Cottrell locks, phase transformation and 9R phase. Our work not only suggests that HEA microfibers have great potential for structural applications in cryogenic environments, but also sheds light on the design of advanced multi-component metallic microfibers with superior mechanical properties.

1. Introduction

With the increasing demand for miniaturized devices, various small-volume structures such as micro-/nanofibers [1–3], thin films [4], and micro-columns [5] are needed in applications including medical implants, avionics, microelectromechanical and cryogenic detector systems [6,7]. Among them, microfibers trigger tremendous interests due to their unique size-dependent properties [8,9]. However, several works have revealed that the influence of sample size on tensile properties was negligible for most traditional microfibers [9–12], and high strengths often come with reduced ductility [13]. Hence, it is necessary to develop microfibers with high strength and large ductility to improve the overall lifetime of the microfibers.

High-/medium-entropy alloys (H/MEAs) are a class of emerging materials with high strength, large ductility, superior fatigue endurance limit and excellent wear resistance [14–18]. In particular, some HEAs with single face-centered cubic (FCC) structure show exceptional tensile properties and fracture toughness at cryogenic temperatures, making them potential candidates for structural applications in extreme environments [18–21]. Despite the potential of HEAs, only limited research

has been hitherto devoted to HEA fibers, and the works carried out were focused mainly on millimeter-fibers [12,22–26]. Fabrication and deformation behaviors of HEA microfibers are largely unexplored [27].

An approach recently found to further achieve enhanced strength and ductility of HEAs is to make heterogeneous gradient microstructures, including gradients in dislocation density, grain size, and hierarchical multiphase structure [28–31]. In addition to superior room temperature mechanical properties, gradient heterogeneous microstructures have been reported to show enhanced fatigue limits [32] and strength-ductility synergy at room temperature [33] and at cryogenic temperatures [34]. The substantial strength-ductility synergy stems from the back-stress strengthening induced by the mechanical incompatibility among heterogeneous domains [29,35]. Here, we select CoCrFeNi HEA as a model material and introduce an ultrafine-grained and heterogeneous microstructure into the cold-drawn CoCrFeNi HEA microfibers through a proper heat treatment. The tensile properties and deformation mechanisms of the CoCrFeNi microfibers at both room temperature (293 K) and cryogenic temperature (150 K) were investigated systematically.

* Corresponding authors.

E-mail addresses: yjhuang@hit.edu.cn (Y. Huang), wenchen@umass.edu (W. Chen).

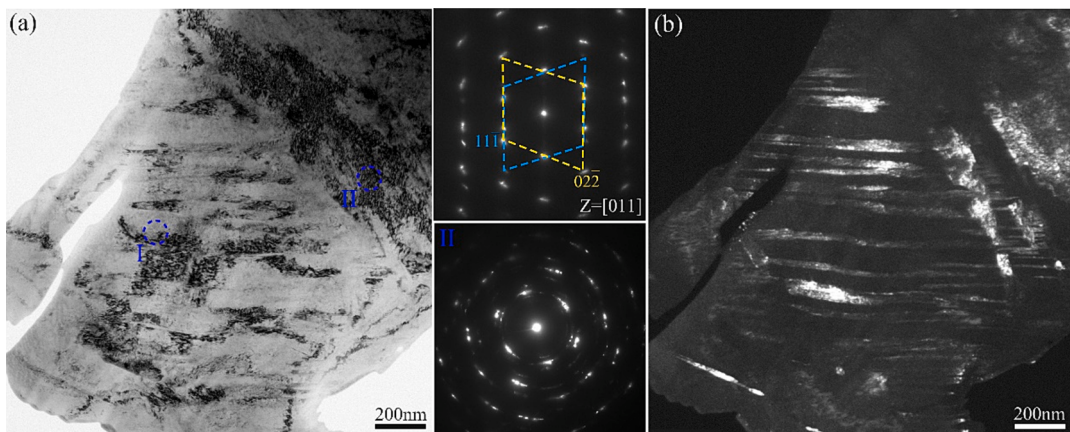
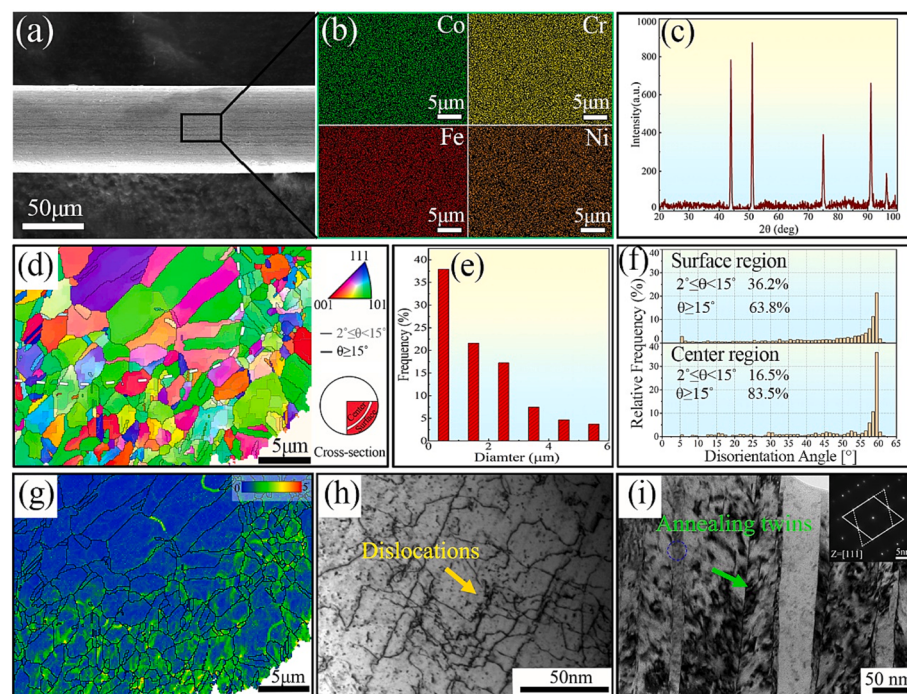


Fig. 1. Typical TEM images of the cold-drawn CoCrFeNi microfiber. (a) The bright field TEM image and the corresponding SAED patterns. (b) Corresponding dark-field TEM image.



2. Experimental

An equimolar CoCrFeNi HEA ingot was fabricated using vacuum induction melting in argon atmosphere from pure Co, Cr, Fe, and Ni metals with purities higher than 99.9 wt% and was remelted at least four times to ensure compositional homogeneity. The ingot was machined into rods with a diameter of 20 mm and a length of 200 mm. The HEA rod was homogenized by annealing at 1473 K for 24 h. The rod was hot-rotary to 8 mm in diameter along the longitudinal direction at 1173 K, and then hot-drawn to 1 mm. Subsequently, the rod was subjected to multi-pass cold-drawing at ambient temperatures. After each drawing step, the cross-sectional area was reduced by ~ 10% and thermal annealing was employed at 1173 K for 1 h. Finally, the initial microfibers with a diameter of ~ 70 μm was obtained. To achieve gradient heterogeneous microstructure with controllable grain sizes, the cold-drawn CoCrFeNi microfibers were heat treated at 1023 K for 1 h in a vacuum furnace.

A series of tensile tests of the HEA microfibers with a gauge length of 10 mm were performed on a DMA Q850 dynamical mechanical analyzer

Fig. 2. (a) SEM image of the annealed CoCrFeNi HEA microfiber. (b) Element distribution maps corresponding to the region highlighted by the black box in (a). (c) XRD pattern. (d) IPF map of annealed microfiber, the grey and black lines correspond to LAGBs ($2^\circ \leq \theta < 15^\circ$) and HAGBs ($\theta \geq 15^\circ$), respectively. (e) The distribution of grain sizes. (f) Misorientation distribution histograms of surface region and center region. (g) KAM map. TEM images of annealed microfiber showing (h) dislocations, and (i) annealing twins.

at 293 K and 150 K with a strain rate of $1 \times 10^{-3} \text{ s}^{-1}$. During the cryogenic tensile tests at 150 K, the sample holder is located in a temperature chamber regulated by liquid nitrogen cooling at a cooling rate of 10 K /min. Microstructural characterization was carried out using a scanning electron microscope (SEM, Zeiss-SUPRA55) equipped with energy-dispersive spectrometry (EDS), electron backscattered diffraction (EBSD) and transmission electron microscope (TEM, Talos F200X). The cross-section of microfibers was prepared for EBSD testing using a cross-section polisher (JEOL IB-09020CP). TEM samples were prepared by focused ion beam (FIB) milling (FEI HELIOS Nano-Lab 600i).

3. Results and discussion

Fig. 1 shows the TEM images of the initial microfiber. The typical bright field TEM image (**Fig. 1a**) shows a large number of the dislocations and deformation twins (DTs) verified by the upper right selected area diffraction pattern (SAED). The bottom right SAED pattern reveals the presence of nano-grains at specific spots (region II) because of the accumulated strain. The corresponding dark-field image (**Fig. 1b**)

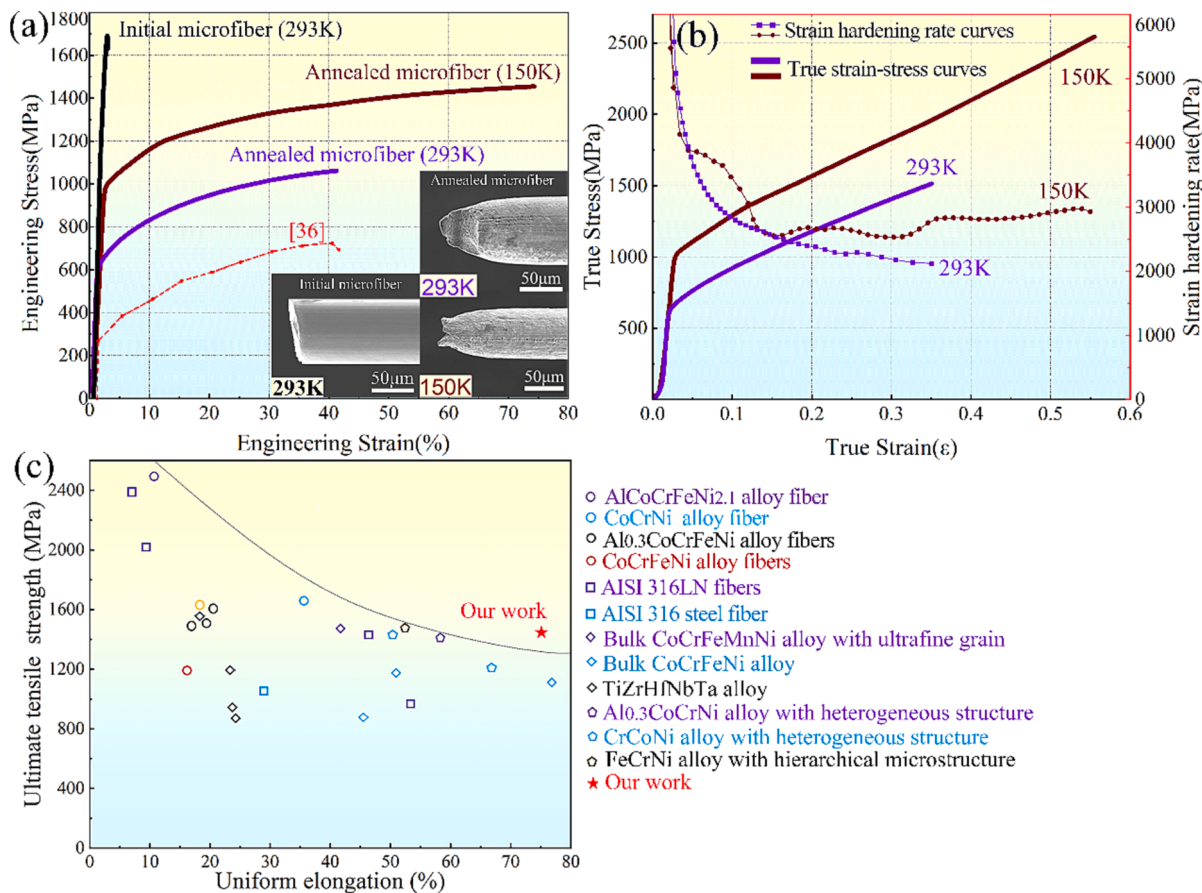


Fig. 3. (a) Engineering tensile stress-strain curves of as-drawn microfibers at 293 K, and annealed microfibers at 293 K and 150 K, with inset highlighting the necking behavior after fracture. (b) True stress-strain and strain hardening rate curves of the annealed HEA microfibers at 293 K and 150 K. (c) Comparison of the ultimate tensile strength and uniform elongation at the cryogenic temperature between the annealed microfibers and other H/MEA fibers [12,22,23,24], traditional metallic fibers [39,40], bulk HEAs [36,41,42,43] and bulk H/MEAs with heterogeneous structures[44,45,46] reported in the literature.

further confirms the existence of elongated twin lamellae with an average width of 40 ± 15 nm.

Fig. 2a shows the SEM image of a typical annealed HEA microfiber. As seen, the annealed microfiber exhibits a consistent diameter of ~ 70 μm with a rather smooth surface. The principal elements of Co, Cr, Fe, and Ni are homogeneously distributed without segregation (Fig. 2b). The XRD pattern only shows single-phase FCC peaks (Fig. 2c), indicating a single-phase FCC solid solution structure for the annealed HEA microfiber. Fig. 2d shows the cross-sectional inverse pole figure (IPF) map of a representative annealed microfiber. The inset shows the location of EBSD analysis area. The grain size and shape exhibit a gradient from the surface to the center of the microfiber and there is no evidence of crystallographic texture. Low-angle grain boundaries (LAGBs) with misorientation angles of $2^\circ \leq \theta < 15^\circ$ and high-angle grain boundaries (HAGBs) with $\theta \geq 15^\circ$ boundaries are illustrated in Fig. 2d, as indicated by grey and black lines. The grain size ranges from 0.25 to 6 μm with a mean value of 1.9 ± 0.3 μm (Fig. 2e). Fig. 2f illustrates the grain boundary misorientation angle distribution histograms of the surface region and center region. It can be seen that the surface region contains more LAGBs compared to the center region. The fractions of HAGBs/LAGBs in the surface region and center region are 68.3%/36.2% and 83.5%/16.5%, respectively. In addition, a sharp peak is evident at 60°, which confirms that the annealed microfiber contains a large fraction of annealing twins. The corresponding Kernel average misorientation (KAM) map in Fig. 2g shows that those grains close to the sample surface have higher KAM values, exhibiting a heterogeneous gradient structure along the radial direction. The gradient structure arises from the cold-drawing process, and the degree of deformation decreases from the

surface towards the center. Since the recrystallization temperature is directly related to the degree of deformation, partially recrystallized microfibers are expected to have inhomogeneous microstructures over the cross-section. After heat treatment at 1023 K for 1 h, the deformed structure is partially recrystallized, resulting in a heterogeneous gradient structure along the radial direction. A typical bright-field TEM image (Fig. 2h) shows that the annealed microfibers possess many dislocations. Some annealing twins are also observed, as also verified by the selected area electron diffraction (SAED) pattern (Fig. 2i).

Fig. 3a depicts the representative engineering tensile stress-strain curves of the as-drawn and annealed CoCrFeNi microfibers, where the tensile curve of the bulk CoCrFeNi HEA in annealed condition is also shown for comparison [36]. With a small decrease in ductility, the annealed microfibers exhibit a much higher strength than the bulk sample. It is noteworthy that the tensile strength of the initial microfiber was 1.7 GPa, which is obviously higher than that obtained from CoCrFeMnNi (1.3 GPa) and Co₁₀Cr₁₅Fe₂₅Mn₁₀Ni₃₀V₁₀ alloys (1.6 GPa) via cold drawing [37,38]. This high tensile strength can be attributed to the significantly high dislocation density, the DTs and presence of nanograins generated by cold drawing. However, the initial microfiber undergoing the cold drawing process shows brittle behavior with negligible ductility due to the presence of high defect density that further declines strain-hardening capability. The 0.2%-offset tensile yield strength (YS), ultimate tensile strength (UTS), and uniform elongation (UE) of annealed microfibers are 600 MPa, 1066 MPa and 42 % at 293 K, and 1010 MPa, 1454 MPa, and 75 % at 150 K, respectively. Apparent necking can be observed after tensile fracture at both 293 K and 150 K (inset in Fig. 3a). Interestingly, while the annealed

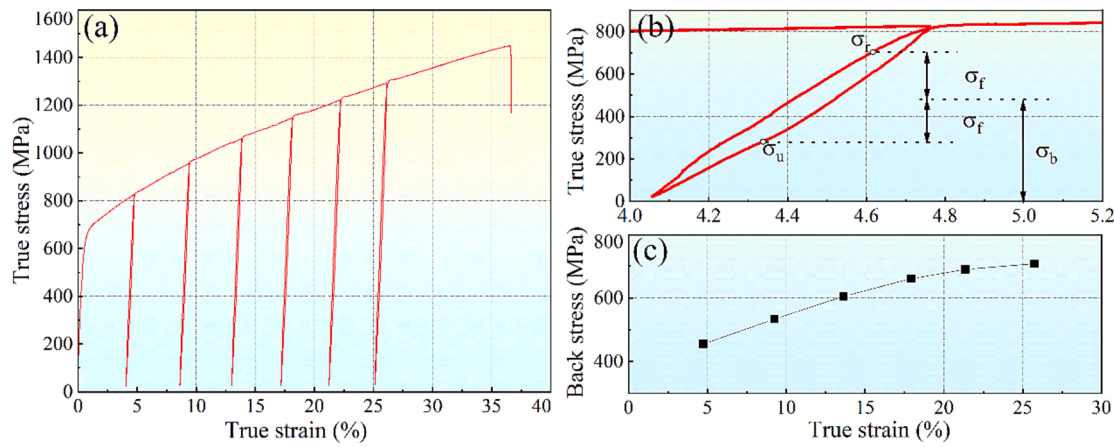


Fig. 4. (a) Loading-unloading-reloading (LUR) true stress–strain curve of annealed CoCrFeNi microfiber at 293 K. (b) A representative LUR cycle showing the hysteresis loop. (c) Back stress evolution of the CoCrFeNi microfiber vary with the true strain.

microfibers are stronger (in terms of YS and UTS) at cryogenic temperature than at room temperature, they are simultaneously more ductile at cryogenic temperature. The annealed CoCrFeNi HEA microfiber shows more pronounced and sustainable strain hardening ability at 150 K, as shown in Fig. 3b. In contrast, the strain hardening rate of annealed microfibers at 293 K exhibits a continuous decrease. To highlight the excellent properties, we compared the tensile strength and uniform elongation of our CoCrFeNi microfibers at the cryogenic temperature with previously reported H/MEA fibers [12,22–24], traditional metallic fibers [39,40], bulk HEAs [36,40,41], and bulk H/MEAs with heterogeneous structures [42–46], as shown in Fig. 3c. The studied microfibers are superior to other alloys in terms of strength-ductility combination, providing great potential for structural applications under extreme conditions.

The annealed CoCrFeNi microfiber presents remarkable combinations of strength and ductility at 293 K and 150 K. Firstly, according to the Hall-Petch relationship, the average grain size of only 1.9 μm

expectedly gives rise to a strengthening effect for the present HEA [47]. Secondly, the annealed microfibers exhibit an inhomogeneous microstructure with varying grain sizes and dislocation densities over the whole cross-section, which causes progressive plastic deformation from the center to the surface during subsequent tensile deformation. To maintain compatibility across the center-(soft)/surface-(hard) interface, heterogeneous deformation occurs in the center grain to avoid formation of voids and material overlap, which generates substantial strain gradients [35,44]. The presence of strain gradient in plastic deformation needs to be accommodated by geometrically necessary dislocations (GNDs) [48,49]. The accumulation of GNDs will cause long-range back stress, that resists forward dislocation motion and leads to back-stress strengthening and pronounced strain hardening [50–52].

In order to evaluate the contribution of the GND-induced back stress to the overall flow stress, tensile tests with a loading–unloading–reloading schedule were conducted at 293 K (Fig. 4a). Pronounced hysteresis loops are observed during the unloading and reloading as

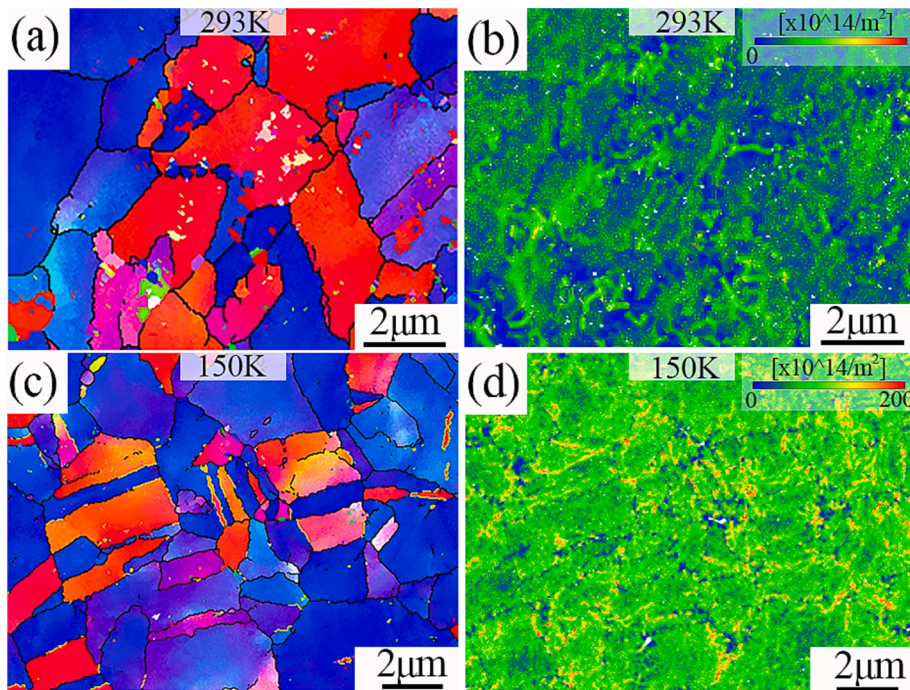


Fig. 5. EBSD images of the annealed CoCrFeNi HEA microfiber after deformation: (a) IPF map for the microfiber deformed at 293 K. (b) IPF map for the microfiber deformed at 150 K. (c) GND map for the microfiber deformed at 293 K. (d) GND map for the microfiber deformed at 150 K.

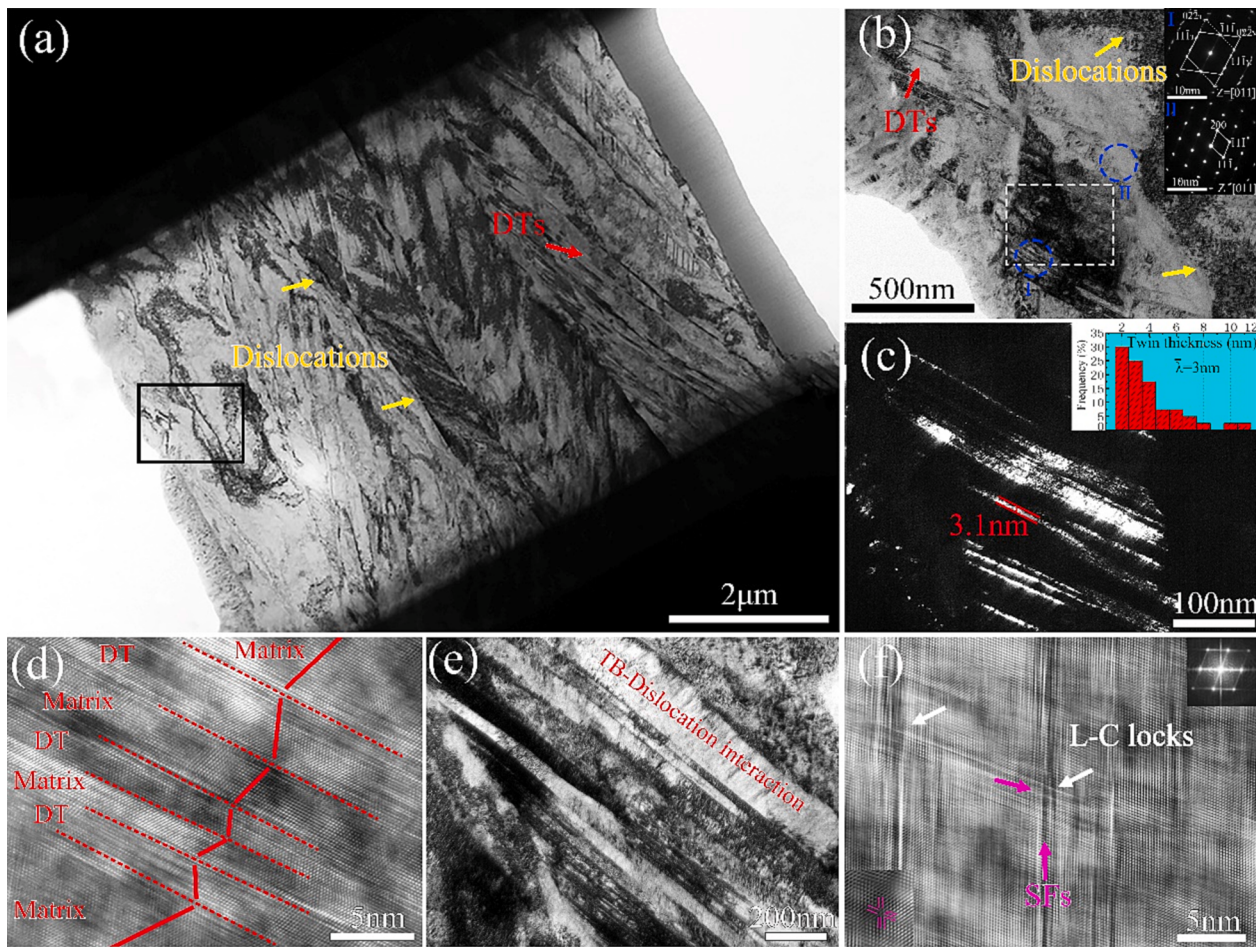


Fig. 6. Typical TEM images of the annealed CoCrFeNi HEA microfiber deformed at 293 K: (a) Low magnitude image. (b) Enlarged image corresponding to the region highlighted by the black box in (a). (c) Higher magnification DF image of dashed rectangular area in (b), and twin thickness distribution (inset). (d) T/M lamellae. (e) Interaction of TBs and dislocations. (f) SFs and L-C locks.

indicated in the example in Fig. 4b which is indicative of a notable Bauschinger effect. The back stress σ_b was calculated by Dickson's method as following [52,53]:

$$\sigma_b = (\sigma_r + \sigma_u)/2 + \sigma_u \quad (1)$$

where σ_u and σ_r denote the yield stress during unloading and reloading, respectively. In the example shown in Fig. 4b, the back stress at a strain of 4.75% reaches as high as 455 MPa, approximately 55% of the flow stress. Fig. 4c shows the variation of the back stresses with true strain. The increases of back stress strengthening result from the accumulation of GNDs. As can be seen, the back stress increases rapidly till 15% strain and then tends to increase slowly up to 740 MPa (~58% of the flow stress). In addition, the strengthening of back stress at cryogenic temperatures has a more significant effect on the increase of flow stress [34]. Consequently, such strong back-stress hardening reflects the beneficial effect of heterogeneous gradient structures.

The deformation microstructure of annealed microfibers after tensile test at 293 K and 150 K are investigated using EBSD (at a step size of 35 nm), as illustrated in Fig. 5a-d. Compared with the original structures, there are large variations in crystallographic orientations within grains in both samples fractured at 293 K and 150 K (Fig. 5a and c). Intragranular lattice curvatures are developed in almost all grains, which implies abundant dislocation activities. The corresponding GND maps as shown in Fig. 5b and Fig. 5d indicate that the density of GNDs in the cryogenic sample is not only higher, but also much more uniform. The average GND densities are calculated to be $2.59 \times 10^{15} \text{ m}^{-2}$ and $7.35 \times 10^{15} \text{ m}^{-2}$ for the 293 K-sample and 150 K-sample, respectively. The

higher GND density and more uniform GND distribution indicate that the gradient structure can better accommodate the high strain gradient, resulting in larger ductility of the HEA microfibers at 150 K [27].

Further microstructural characterization was performed by TEM analysis on the tensile annealed specimens. The deformation substructures at 293 K are shown in Fig. 6. At a low magnification and a high magnification as depicted in Fig. 6a and 6b, respectively, dislocations are the main deformation substructures, and a small amount of DTs are observed, similar to bulk HEAs deformed at ambient temperature [41]. The DF image in Fig. 6c, which corresponds to the region indicated by the dashed white rectangle in Fig. 6b, shows a bundle of DTs with an average thickness of ~3 nm in bright contrast. The high-resolution TEM (HRTEM) further shows fine lamellae of twins and matrix (Fig. 6d), which could provide more boundaries to block dislocation motions, leading to prominent strain-hardening behavior [54]. As shown in the bright field image in Fig. 6e, there is a strong interaction between twins, as well as between twin boundaries and dislocations. Furthermore, dense stacking faults (SFs) on multiple {111} planes are observed as shown in Fig. 6f. At the intersections of the SFs on different {111} planes, Lomer-Cottrell (L-C) locks are often observed, as shown by the high-resolution image in the inset of Fig. 6f. A high density of L-C locks which are sessile, "stair-rod" edge dislocations at intersections of {111} planes provide strong barriers to pin and entrap dislocations, thus further enhancing the strain-hardening capacity [55].

Next, we discuss the deformation microstructures of the annealed CoCrFeNi microfiber at 150 K. In contrast to the annealed microfiber deformed at 293 K, extensive dislocations, SFs, L-C locks and twinning

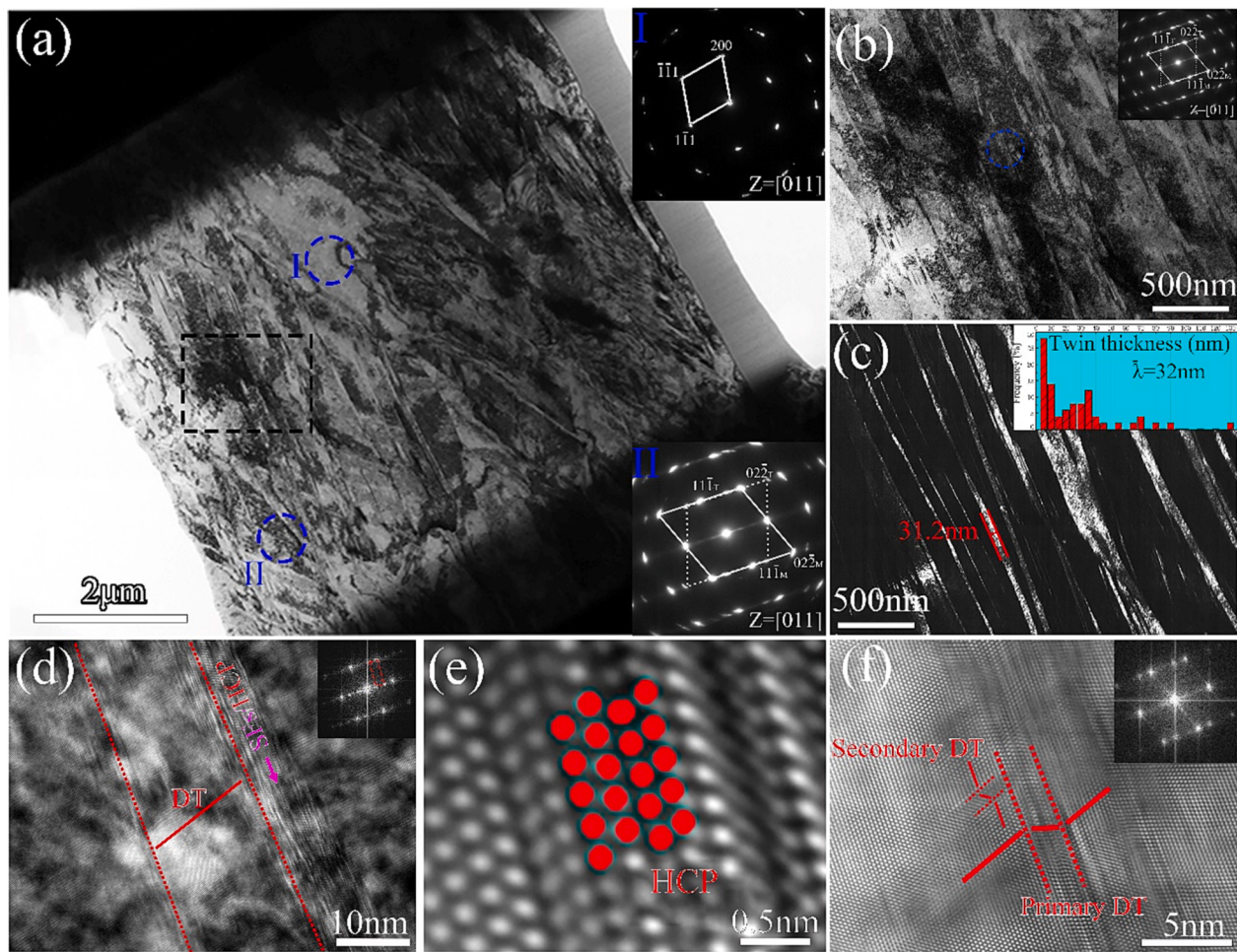


Fig. 7. Typical TEM images of the annealed CoCrFeNi HEA microfiber deformed at 150 K: (a) Magnitude image and SAED pattern showing diffraction spots from regions I and II (inset). (b) Enlarged image corresponding to the region highlighted by the black box in (a). (c) DF image corresponding to (b), and twin thickness distribution (inset). (d) The lamellar structure of DT, SFs and HCP. (e) High magnification image of area in d showing the HCP stacking. (f) Secondary DTs.

activities have been observed in microfiber deformed at 150 K (Fig. 7). These related diffraction spots are verified from the SAED (see inset of Fig. 7a). Much more significant twin-dislocation interactions can be observed in 150 K-sample (Fig. 7b). The DF image (Fig. 7c) corresponding to Fig. 7b reveals that the average twin width is 32 nm, which can be possibly attributed to the merging of nanotwins with increasing strain after deformation twinning. In addition, we also observed a special lamellar structure in the 150 K sample, composed of FCC matrix, twin, and HCP nanolayers, as shown in Fig. 7d. Fig. 7e shows the HCP stacking with four atomic layers. Recent researchs have shown that the HCP structure can be readily transformed locally from the FCC structure by introducing SFs [56]. Therefore, the stacking fault energy (SFE) plays a significant role in the FCC-to-HCP transformation, and the SFE shows a large positive temperature dependence. This structure is often observed in the deformed structure of HEAs with low SFE [57,58], especially at low temperatures. Such structures can act as effective barriers for dislocation slip, and DT could be thickened through consuming newly formed SFs/hcp lamellar during deformation [59]. It is worth mentioning that the quantity of the DT-SFs-HCP lamellar structure is insignificant throughout the whole sample. Therefore, it should not be the most vital contributing factor in enhancing the strength of CoCrFeNi fibers at 150 K. Additionally, the HRTEM image shown in Fig. 7d exhibits the existence of secondary twins. It has been reported that the existence of multiple twinning systems can provide sufficient pathways for easy glide and make cross-slip move from one boundary to another, so that larger plastic deformation gets coordinated

and higher strain hardening capacity is obtained [18].

Generally, the ease of deformation twinning is related to the critical stress for twinning (σ_{tw}), which can be estimated by [60]:

$$\sigma_{tw} = \left(\frac{\gamma}{b} + \frac{K_{tw}^{H-P}}{\sqrt{d}} \right) M \quad (2)$$

where γ is the SFE (32.5 mJ/m² at 293 K, and 7.4 mJ/m² at 140 K) [61], b is the Burgers vector length ($b = 0.252$ nm), K_{tw}^{H-P} is the Hall-Petch constant for twinning ($K_{tw}^{H-P} = 464$ MPa μm^{1/2}) [62], d is the grain size, and M is the Taylor factor ($M = 3.06$). Then σ_{tw} was estimated to be 1402 MPa at 293 K, and 1320 MPa at 150 K. Therefore, for the 150 K-sample, DTs occurred in the early stage of deformation (~11.3 % of true strain). In contrast, for the annealed 293 K-sample, DTs formed only in the final stage of deformation (~32 % of true strain), prior to final fracture, as shown in Fig. 3b.

In addition to aforementioned mechanisms, two other types of DT activities were found in the annealed microfiber deformed at 150 K. The first was formed through the migration of 9R-phase mediated $\Sigma_3\{112\}$ incoherent twin boundaries [63], as exhibited in Fig. 8a. The upper of Fig. 8c shows clearly that the 9R phase, as verified by the fast Fourier transformation (FFT) pattern, is composed of SF bands with repeating units of 9 {111} atomic layers. It is well known that the $\Sigma_3\{112\}$ incoherent twin boundary (ITB) presents a set of Shockley partial dislocations with a repeatable sequence of b_2 : b_1 : b_3 on successive (111) planes ($b_1 + b_2 + b_3 = 0$) [64,65]. Due to the Peierls barriers acting on

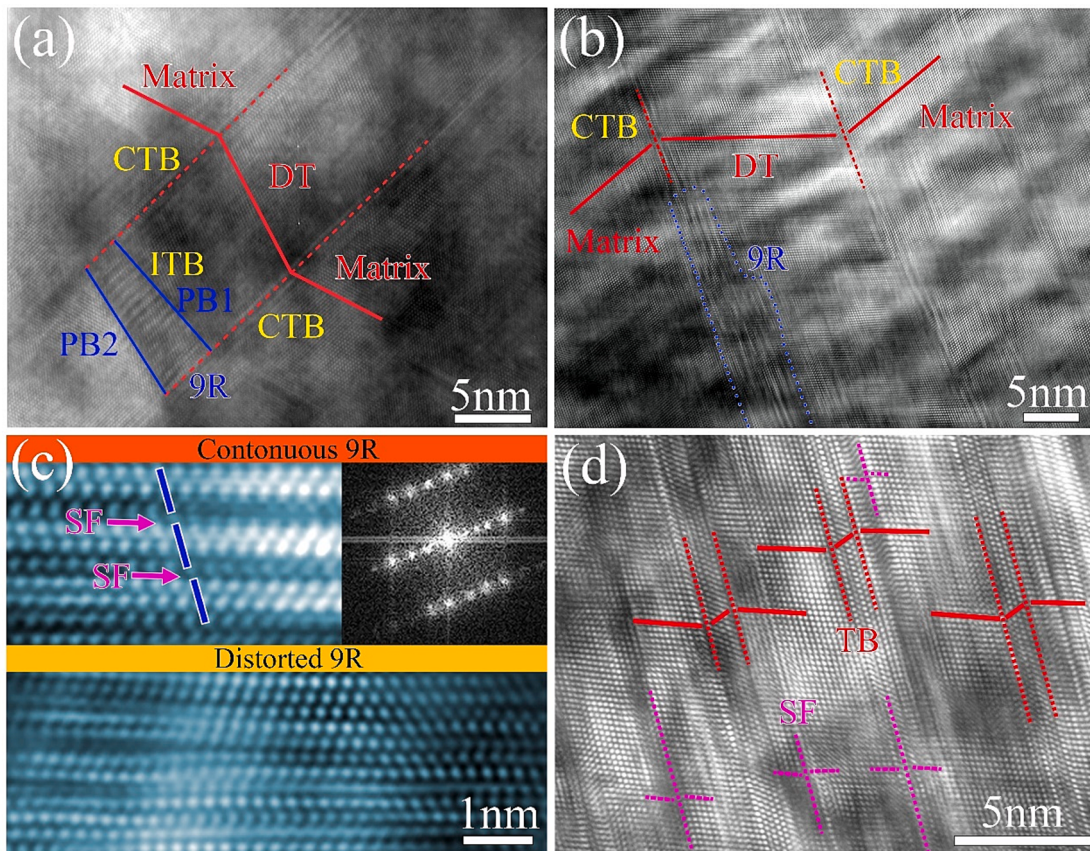


Fig. 8. Two other types of twinning mechanisms: (a) The twin mediated by 9R phase. (b) A step 9R structure (c) Continuous 9R and corresponding FFT pattern (upper) and distortion 9R (lower). (d) Numerous DTs and SF-decorated TBs.

the paired partials b₂ and b₃ were higher than that acting on the partial dislocation b₁, leading to the other two partial dislocations b₂ and b₃ retained in their initial positions, while the partial dislocation b₁ of ITB moved ahead under the tensile loading. This leads to the ITB dissociation into two tilt boundaries (PB1 and PB2), bonding a 9R phase. The resulting SFs and the interactions among the three partials will pull the paired partials b₂ and b₃ to approach b₁. This process could self-repeat and cause the migration of ITBs (i.e., the 9R phase) to the matrix direction and subsequently the growth of the DT [66]. The propagation of the ITBs destroys the coherency of the coherent twin boundaries (CTBs), and propagation directions of the ITBs will determine the occurrence of twinning or detwinning [67], as shown in Fig. 8b. In general, the grain size plays a critical role in the formation of the 9R phase. As proposed by Shi et al., the 9R phase and its mediated DT are activated in relatively-small FCC grains [64]. In addition, the formation of 9R phase is closely related to the SFE (low SFE can promote the nucleation of ITBs), and the 9R phase is rarely detected in medium-to-high SFE materials, like Al even under high shear stresses [68]. Therefore, the studied CoCrFeNi microfibers with a low SFE and ultrafine grains promotes the activation of 9R phase and its mediated DT. We noticed that in the studied CoCrFeNi microfibers, a large number of defects, such as dislocations and SFs are found in front of the 9R phase. Previous research has revealed that the complex interaction between 9R phase and these defects leads to the evolution from continuous 9R to the distorted 9R (Fig. 8b and lower of Fig. 8c), which can contribute to substantial strain hardening during deformation [64,69].

Fig. 8d shows twins formed by another twinning mechanism, which is characterized by multiple SF-decorated twin boundaries [28,64]. The Shockley partial dislocations (Burgers vectors $1/6 \langle 112 \rangle$) emitted on (111) glide planes, leaving behind multiple SFs. These multiple SFs expanded under high stresses, increasing their energy and making their

transformation to a twin energetically favorable. Such extremely-fine SFs and twins not only effectively mediated plastic strains, exhibiting SF-induced plasticity, but also promoted considerable strengthening and strain-hardening [64]. Significantly, the activation of two twinning mechanisms usually required high flow stresses, so those twins could be detected in nanograins or during the deformation of micro-/macrograins under high strain rates or at low temperatures [28]. In the annealed HEA microfibers, both the heterogeneous gradient structure and low-temperature deformation elevated the local flow stress. Hence, activation of multiple DTs was considered to be the dominant mechanism for the more superior tensile properties of annealed microfiber deformed at 150 K.

4. Conclusions

In summary, the annealed CoCrFeNi HEA microfibers, with an ultrafine grain and heterogeneous gradient structures are fabricated. The annealed microfiber exhibits an unprecedented strength-ductility synergy both at 293 K and 150 K. Especially at 150 K, it displays an ultrahigh YS of ~ 1 GPa, UTS of 1.45 GPa and outstanding UE of 75%. The outstanding mechanical properties with high YS of 600 MPa, UTS of 1066 MPa and UE of 42% are achieved at 293 K as well. Excellent tensile properties of annealed microfiber can be attributed to grain size strengthening, back-stress hardening induced by inhomogeneous microstructures, as well as a transition from a single mechanism of dislocation slip at 293 K to DT-dominated multiple mechanisms of dislocation, SFs, L-C locks, HCP phase transformation and 9R phase at 150 K. Furthermore, two other types of twinning mechanisms are activated, which are SF-decorated DTs and 9R-phase mediated DTs. This work can provide fundamental insights into the intrinsic mechanisms underlying the excellent performance of HEA microfibers under

different temperatures, and present an attractive reference to manufacture high performance HEA microfibers for broad applications.

Declaration of Competing Interest

The authors declare that they have no known competing financial interests or personal relationships that could have appeared to influence the work reported in this paper.

Data availability

Data will be made available on request.

Acknowledgements

The authors would like to acknowledge the financial support from the National Natural Science Foundation of China under Grant Nos. 52171154, 52071118, and 51901151 and Interdisciplinary Research Foundation of HIT under Grant No. IR2021201.

References

- [1] W. Yan, I. Richard, G. Kurtuldu, N.D. James, G. Schiavone, J.W. Squair, T. Nguyen-Dang, T. Das Gupta, Y. Qu, J.D. Cao, R. Ignatans, S.P. Lacour, V. Tileli, G. Courtine, J.F. Löffler, F. Sorin, *Nat. Nanotechnol.* 15 (2020) 875–882, <https://doi.org/10.1038/s41565-020-0747-9>.
- [2] Y.J. Chen, X.H. An, X.Z. Liao, *Appl. Phys. Rev.* 4 (2017), 031104, <https://doi.org/10.1063/1.4989649>.
- [3] S. Wang, Z. Shan, H. Huang, *Adv. Sci.* 4 (2017) 1600332, <https://doi.org/10.1002/advs.2016000332>.
- [4] Y.Q. Fu, J.K. Luo, N.T. Nguyen, A.J. Walton, A.J. Flewitt, X.T. Zu, Y. Li, G. McHale, A. Matthews, E. Iborra, H. Du, W.I. Milne, *Prog. Mater Sci.* 89 (2017) 31–91, <https://doi.org/10.1016/j.pmatsci.2017.04.006>.
- [5] M.D. Uchic, D.M. Dimiduk, J.N. Florando, W.D. Nix, *Science* 305 (5686) (2004) 986–989, <https://doi.org/10.1126/science.1098993>.
- [6] C.A. Allen, D.E. Franz, S.H. Moseley, *J. Vac. Sci. Technol. A* 24 (4) (2006) 1552–1555, <https://doi.org/10.1116/1.2194922>.
- [7] H.X. Zhu, J. Jia, W. Liu, D. Jiang, Z.X. Li, Z.L. Shi, Q.N. Cui, B. Liu, C.X. Xu, *Appl. Phys. Lett.* 122 (2023), 234101, <https://doi.org/10.1063/5.0147253>.
- [8] Y. Chen, O. Kraft, M. Walter, *Acta Mater.* 87 (2015) 78–85, <https://doi.org/10.1016/j.actamat.2014.12.034>.
- [9] D. Liu, Y. He, D.J. Dunstan, B. Zhang, Z. Gan, P. Hu, H. Ding, *Int. J. Plast.* 41 (2013) 30–52, <https://doi.org/10.1016/j.ijplas.2012.08.007>.
- [10] N.A. Fleck, G.M. Muller, M.F. Ashby, J.W. Hutchinson, *Acta Metall. Mater.* 42 (1994) 475–487, [https://doi.org/10.1016/0956-7151\(94\)90502-9](https://doi.org/10.1016/0956-7151(94)90502-9).
- [11] D. Liu, Y. He, D.J. Dunstan, B. Zhang, Z. Gan, P. Hu, H. Ding, *Phys. Rev. Lett.* 110 (2013), 244301, <https://doi.org/10.1103/PhysRevLett.110.244301>.
- [12] D.Y. Li, C.X. Li, T. Feng, Y.D. Zhang, G. Sha, J.J. Lewandowski, P.K. Liaw, Y. Zhang, *Acta Mater.* 123 (2017) 285–294, <https://doi.org/10.1016/j.actamat.2016.10.038>.
- [13] F. Fang, L.C. Zhou, X.J. Hu, X.F. Zhou, Y.Y. Tu, Z.H. Xie, J.Q. Jiang, *Mater. Des.* 79 (2015) 60–67, <https://doi.org/10.1016/j.matdes.2015.04.036>.
- [14] J.W. Yeh, S.K. Chen, S.J. Lin, J.Y. Gan, T.S. Chin, T.T. Shun, C.H. Tsau, S.Y. Chang, *Adv. Eng. Mater.* 6 (5) (2004) 299–303, <https://doi.org/10.1002/adem.200300567>.
- [15] B. Cantor, *Prog. Mater Sci.* 120 (2021), 100754, <https://doi.org/10.1016/j.pmatsci.2020.100754>.
- [16] H.G. Li, P.C. Che, X.K. Yang, Y.J. Huang, Z.L. Ning, J.F. Sun, H.B. Fan, *Rare Metals.* 41 (2022) 1210–1216, <https://doi.org/10.101007/s12598-021-01867-1>.
- [17] H.G. Li, Y.J. Huang, J.F. Sun, Y.Z. Lu, J. Mater. Sci. Technol. 77 (2021) 187–195. Doi: 10.1016/j.jmst.2020.10.052.
- [18] W.D. Li, D. Xie, D.Y. Li, Y. Zhang, Y.F. Gao, P.K. Liaw, *Prog. Mater Sci.* 118 (2021), 100777, <https://doi.org/10.1016/j.pmatsci.2021.100777>.
- [19] F. Otto, A. Dlouhy, C. Somsen, H. Bei, G. Eggeler, E.P. George, *Acta Mater.* 61 (15) (2013) 5743–5755, <https://doi.org/10.1016/j.actamat.2013.06.018>.
- [20] B. Gludovatz, A. Hohenwarter, D. Catoor, E.H. Chang, E.P. George, R.O. Ritchie, *Science* 345 (6201) (2014) 1153–1158, <https://doi.org/10.1126/science.1254581>.
- [21] X.Z. Zhong, Q.M. Zhang, M.Z. Ma, J. Xie, M.Z. Wu, S.Y. Ren, Y.M. Yan, *Mater. Des.* 219 (2022), 110724, <https://doi.org/10.1016/j.matdes.2022.110724>.
- [22] J.P. Liu, J.X. Chen, T.W. Liu, C. Li, Y. Chen, L.H. Dai, *Scr. Mater.* 181 (2020) 19–24, <https://doi.org/10.1016/j.scriptamat.2020.02.002>.
- [23] W.Y. Huo, F. Fang, H. Zhou, Z.H. Xie, J.K. Shang, J.Q. Jiang, *Scr. Mater.* 141 (2017) 125–128, <https://doi.org/10.1016/j.scriptamat.2017.08.006>.
- [24] J.X. Chen, T. Li, Y. Chen, F.H. Cao, H.Y. Wang, L.H. Dai, *Acta Mater.* 243 (2023), 118515, <https://doi.org/10.1016/j.actamat.2022.118515>.
- [25] S.C. Zhou, C.D. Dai, H.X. Hou, Y.P. Lu, P.K. Liaw, Y. Zhang, *Scr. Mater.* 226 (2023), 115234, <https://doi.org/10.1016/j.scriptamat.2022.115234>.
- [26] Y. Qiao, F.H. Cao, Y. Chen, H.Y. Wang, L.H. Dai, *Mater. Sci. Eng. A* 856 (2022), 144041, <https://doi.org/10.1016/j.msea.2022.144041>.
- [27] J.X. Chen, Y. Chen, J.P. Liu, T.W. Liu, L.H. Dai, *Scr. Mater.* 199 (2021), 113897, <https://doi.org/10.1016/j.scriptamat.2021.113897>.
- [28] Q.S. Pan, L.X. Zhang, R. Feng, Q.H. Lu, K. An, A.C. Chuang, J.D. Poplawsky, P. K. Liaw, L. Lu, *Science* 374 (6570) (2021) 984–989, <https://doi.org/10.1126/science.abj8114>.
- [29] S.W. Wu, G. Wang, Q. Wang, Y.D. Jia, J. Yi, Q.J. Zhai, J.B. Liu, B.A. Sun, H.J. Chu, J. Shen, P.K. Liaw, C.T. Liu, T.Y. Zhang, *Acta Mater.* 165 (2019) 444–458, <https://doi.org/10.1016/j.actamat.2018.12.012>.
- [30] S.H. Shim, H. Pouraliakbar, B.J. Lee, Y.K. Kim, M.S. Rizi, S.I. Hong, *Mater. Sci. Eng. A* 853 (2022), 143729, <https://doi.org/10.1016/j.msea.2022.143729>.
- [31] S.H. Shim, H. Pouraliakbar, B.J. Lee, Y.K. Kim, M.S. Rizi, S.I. Hong, *Data Brief* 45 (2022), 108567, <https://doi.org/10.1016/j.dib.2022.108567>.
- [32] K. Zhang, Z.B. Wang, K. Lu, *Mater. Res. Lett.* 5 (2016) 258–266, <https://doi.org/10.1080/21663831.2016.1253625>.
- [33] S.H. Shim, H. Pouraliakbar, H. Minouei, M.S. Rizi, V. Fallah, Y.S. Na, J.H. Han, S. I. Hong, *J. Alloy. Compd.* 954 (2023), 170091, <https://doi.org/10.1016/j.jallcom.2023.170091>.
- [34] J. Moon, J.M. Park, J.W. Bae, N. Kang, J. Oh, H. Shin, H.S. Kim, *Scr. Mater.* 186 (2020) 24–28, <https://doi.org/10.1016/j.scriptamat.2020.04.044>.
- [35] M.N. Hasan, Y.F. Liu, X.H. An, J. Gu, M. Song, Y. Cao, Y.S. Li, Y.T. Zhu, X.Z. Liao, *Int. J. Plast.* 123 (2019) 178–195, <https://doi.org/10.1016/j.ijplas.2019.07.017>.
- [36] Z. Wu, H. Bei, G.M. Pharr, E.P. George, *Acta Mater.* 81 (2014) 428–441, <https://doi.org/10.1016/j.actamat.2014.08.026>.
- [37] H.S. Cho, S.J. Bae, Y.S. Na, K.S. Lee, J.H. Kim, D.G. Lee, *J. Alloy. Compd.* 821 (2020), 153526, <https://doi.org/10.1016/j.jallcom.2019.153526>.
- [38] X.G. Ma, J. Chen, X.H. Wang, Y.J. Xu, Y.J. Xue, *J. Alloy. Compd.* 795 (2019) 45–53, <https://doi.org/10.1016/j.jallcom.2019.04.296>.
- [39] I. Volokitina, A. Volokitin, A. Denissova, T. Fedorova, D. Lawrinuk, A. Kolesnikov, A. Yerzhanov, Y. Kuatbay, Y. Liseitsev, *Case Stud. Constr. Mater.* 19 (2023) e02346.
- [40] P. Czarkowski, A.T. Krawczyńska, T. Brynk, M. Nowacki, M. Lewandowska, K. J. Kurzydłowski, *Cryogenics* 64 (2014) 1–4, <https://doi.org/10.1016/j.cryogenics.2014.07.014>.
- [41] S.J. Sun, Y.Z. Tian, X.H. An, H.R. Lin, J.W. Wang, Z.F. Zhang, *Mater. Today Nano* 4 (2018) 46–53, <https://doi.org/10.1016/j.mtnano.2018.12.002>.
- [42] J.P. Liu, X.X. Guo, Q.Y. Lin, Z.B. He, X.H. An, L.F. Li, P.K. Liaw, X.Z. Liao, L.P. Yu, J.P. Lin, L. Xie, J.L. Ren, Y. Zhang, *Sci. China Mater.* 62 (2019) 853–863, <https://doi.org/10.1007/s04843-018-9373-y>.
- [43] S.B. Wang, M.X. Wu, D. Shu, G.L. Zhu, D.H. Wang, B.D. Sun, *Acta Mater.* 201 (2020) 517–527, <https://doi.org/10.1016/j.actamat.2020.10.044>.
- [44] P. Sathiyamoorthy, P. Asghari-Rad, J.M. Park, J. Moon, J.W. Bae, A. Zargaran, H. S. Kim, *Mater. Sci. Eng. A* 766 (2019), 138372, <https://doi.org/10.1016/j.msea.2019.138372>.
- [45] B. Gan, J.M. Wheeler, Z. Bi, L. Liu, J. Zhang, H. Fu, J. Mater. Sci. Technol. 35 (2019) 957–961, <https://doi.org/10.1016/j.jmst.2018.12.002>.
- [46] Z.H. Xie, A. Fu, H. Duan, B.F. Wang, X.F. Li, Y.K. Cao, B. Liu, *Intermetallics* 160 (2023), 107945, <https://doi.org/10.1016/j.intermet.2023.107945>.
- [47] D.X. Wei, W. Gong, T. Tsuru, T. Kawasaki, S. Harjo, B. Cai, P.K. Liaw, H. Kato, *Int. J. Plast.* 158 (2022), 103417, <https://doi.org/10.1016/j.ijplas.2022.103417>.
- [48] P. Sathiyamoorthy, H.S. Kim, *Prog. Mater Sci.* 123 (2022), 100709, <https://doi.org/10.1016/j.pmatsci.2020.100709>.
- [49] X.Y. Li, L. Lu, J.G. Li, X. Zhang, H.J. Gao, *Nat. Rev. Mater.* 5 (2020) 706–723, <https://doi.org/10.1038/s41578-020-0212-2>.
- [50] X.H. An, *Science* 373 (2021) 857–858, <https://doi.org/10.1126/science.abk1671>.
- [51] H.K. Park, K. Ameyama, J. Yoo, H. Hwang, H.S. Kim, *Math. Res. Lett.* 6 (5) (2018) 261–267, <https://doi.org/10.1080/21663831.2018.1439115>.
- [52] M.X. Yang, Y. Pan, F.P. Yuan, Y.T. Zhu, X.L. Wu, *Mater. Res. Lett.* 4 (3) (2016) 145–151, <https://doi.org/10.1080/21663831.2016.1153004>.
- [53] J.I. Dickson, J. Boutin, L. Handfield, *Mater. Sci. Eng. A* 64 (1) (1984) L7–L11, [https://doi.org/10.1016/0025-5416\(84\)90083-1](https://doi.org/10.1016/0025-5416(84)90083-1).
- [54] T.K. Liu, Z. Wu, A.D. Stoica, Q. Xie, W. Wu, Y.F. Gao, H. Bei, K. An, *Mater. Des.* 131 (2017) 419–427, <https://doi.org/10.1016/j.matdes.2017.06.039>.
- [55] Y. Cao, S. Ni, X.Z. Liao, M. Song, Y.T. Zhu, *Mater. Sci. Eng. R* 133 (2018) 1–59, <https://doi.org/10.1016/j.mser.2018.06.001>.
- [56] S. Liu, X. Sun, Y.Z. Tian, X.H. An, W. Li, Y.J. Chen, G.L. Zhang, L. Vitos, *PNAS Nexus* 2: 1 (2022) pgac282, <https://doi.org/10.1093/pnasnexus/pgac282>.
- [57] Q.Y. Lin, J.P. Liu, X.H. An, H. Wang, Y. Zhang, X.Z. Liao, Mater. Res. Lett. 6 (4) (2018) 236–243, <https://doi.org/10.1080/21663831.2018.1434250>.
- [58] Y.J. Chen, D.K. Chen, X.H. An, Y. Zhang, Z.F. Zhou, S. Lu, P. Munroe, S. Zhang, X. Z. Liao, T. Zhu, Z.H. Xie, *Acta Mater.* 215 (2021), 117112, <https://doi.org/10.1016/j.actamat.2021.117112>.
- [59] D. Huang, Y.X. Zhuang, *Mater. Des.* 223 (2022), 111212, <https://doi.org/10.1016/j.matdes.2022.111212>.
- [60] I. Gutierrez-Urrutia, S. Zaeferer, D. Raabe, *Mater. Sci. Eng. A* 527 (15) (2010) 3552–3560, <https://doi.org/10.1016/j.msea.2010.02.041>.
- [61] W. Woo, M. Naeem, J.S. Jeong, C.M. Lee, S. Harjo, T. Kawasaki, H. He, X.L. Wang, *Mater. Sci. Eng. A* 781 (2020), 139224, <https://doi.org/10.1016/j.msea.2020.139224>.
- [62] J. Yang, J.W. Qiao, S.G. Ma, G.Y. Wu, D. Zhao, Z.H. Wang, *J. Alloy. Compd.* 795 (2019) 269–274, <https://doi.org/10.1016/j.jallcom.2019.04.333>.
- [63] X.H. An, M. Song, Y. Huang, X.Z. Liao, S.P. Ringer, T.G. Langdon, Y.T. Zhu, *Scr. Mater.* 72–73 (2014) 35–38, <https://doi.org/10.1016/j.scriptamat.2013.10.014>.
- [64] P.J. Shi, Y.B. Zhong, Y. Li, W.L. Ren, T.X. Zheng, Z. Shen, B. Yang, J.C. Peng, P. F. Hu, Y. Zhang, P.K. Liaw, Y.T. Zhu, *Mater. Today* 41 (2020) 62–71, <https://doi.org/10.1016/j.mattod.2020.09.029>.

- [65] H. Wang, D.K. Chen, X.H. An, Y. Zhang, X.Z. Liao, S.J. Sun, Y.Z. Tian, Z.F. Zhang, A.G. Wang, M. Song, S.P. Pinger, T. Zhu, X.Z. Liao, Sci. Adv. 7 (14) (2021) eabe3105. DOI: 10.1126/sciadv.abe3105.
- [66] J. Gu, L.X. Zhang, S. Ni, M. Song, Scr. Mater. 125 (2016) 49–53, <https://doi.org/10.1016/j.scriptamat.2016.08.006>.
- [67] Q. Li, S. Xue, J. Wang, S. Shao, A.H. Kwong, A. Giwa, Z. Fan, Y. Liu, Z. Qi, J. Ding, H. Wang, J.R. Greer, H. Wang, X. Zhang, Adv. Mater. 30 (2018) 1704629, <https://doi.org/10.1002/adma.201704629>.
- [68] X.Y. Liu, C.L. Liu, M. Chen, Y.Z. Gao, L.X. Wei, X.H. Peng, X.F. Zhang, Mater. Des. 229 (2023), 111925, <https://doi.org/10.1016/j.matdes.2023.111925>.
- [69] J.D. Zuo, C. He, M. Cheng, K. Wu, Y.Q. Wang, J.Y. Zhang, G. Liu, J. Sun, Acta Mater. 174 (2019) 279–288, <https://doi.org/10.1016/j.actamat.2019.05.053>.